Journal of The Electrochemical Society

OPEN ACCESS

Tracking the Lifecycle of a 21700 Cell: A 4D Tomography and Digital Disassembly Study

To cite this article: Matt D. R. Kok *et al* 2023 *J. Electrochem. Soc.* **170** 090502

Journal of The Electrochemical Society, 2023 **170** 090502

Tracking the Lifecycle of a 21700 Cell: A 4D Tomography and Digital Disassembly Study

Matt D. R. Kok,[1] Anmol Jnawali,[1] Thomas M. M. Heenan,[1] Thomas G. Tranter,[1] Dan J.L. Brett,[1,2,3] Paul R. Shearing,[1,2,3] and James B. Robinson[1,2,3,z]

[1]*Electrochemical Innovation Lab, Department of Chemical Engineering, UCL, London, WC1E 7JE, United Kingdom*
[2]*Advanced Propulsion Lab, Department of Chemical Engineering, UCL, London, E20 2AE, United Kingdom*
[3]*The Faraday Institution, Quad One, Harwell Science and Innovation Campus, Didcot, OX11 0RA, United Kingdom*

Extending the lifetime of commercial Li-ion cells is amongst the most important challenge to facilitate the continued electrification of transport as demonstrated by the substantial volume of literature dedicated to identifying degradation mechanisms in batteries. Here, we conduct a long-term study on a cylindrical Li-ion cell, tracking the evolution of the structure of the cell using X-ray computed tomography. By evaluating the internal geometry of the cell over several hundreds of cycles we show a causal relationship between changes in the electrode structure and the capacity fade associated with cell ageing. The rapid aging which occurs as cells reach their end-of-life condition is mirrored in a significant acceleration in internal architecture changes. This work also shows the importance of consistent and accurate manufacturing processes with small defects in the jelly-roll being shown to act as nucleation sites for the structural degradation and by extension capacity fade.
 [DOI: 10.1149/1945-7111/acf412]

Manuscript submitted June 30, 2023; revised manuscript received August 18, 2023. Published September 4, 2023. *This paper is part of the JES Focus Issue on Journey of Lithium-Ion: Performance, Safety, and Lifespan.*

Lithium ion (Li-ion) batteries are established as the pre-eminent technology for clean energy storage. As the world continues to electrify personal transportation the market for commercial lithium-ion batteries will continue to expand. The worldwide production of Li-ion batteries was 297 GWh·year^{-1} in 2018, by 2028 it is expected to increase by five times to 1.6 TWh·year^{-1}.[1] These market forces have rapidly increased the research being performed on commercial cells; understanding how the cells currently in circulation perform and degrade will help shape the next generation of cell design. A significant research aims to understand how the cell ages over time, and ultimately whether capacity fade can be predicted or mitigated.

Commonly, aging studies look at the effect of operational parameters on cell lifetime performance. These parameters may be depth of discharge,[2] operational temperature,[3,4] cycling rate,[5] or combinations of the three.[6–8] Another set of studies have investigated electrochemical signals that pre-empt cell failure. Severson et al. leveraged machine-learning on early cycle voltage discharge curves to predict eventual capacity degradation,[9] while Zhang et al. performed a similar study using impedance spectra.[10] Recently, studies have investigated the interplay between the macrostructure in the cell and the capacity loss: Waldmann et al. looked at the effect of the cell's overall design specifically whether there was a central pin in the jelly-roll, on how the cell degraded and deformed,[11] and Willenberg et al. monitored the volume change of the commercial Li-ion cells over time with cycling.[12] In both cases significant structural deformations were found to evolve with time, linking electrochemical performance to the macroscopic battery structures. In a similar vein, Pfrang et al. found geometric inhomogeneities as the major cause for mechanical failure for commercial 18650 cells[13,14] and Bach et al. linked heterogeneous compression in the jelly-roll to non-linear cell aging.[15] A study by Carter et al. suggested that jelly roll collapse was the primary mode of degradation in a Li-ion cells that had been operated at low temperatures.[16] The authors later examined the impact of the wiring configuration of LiFePo4 cells identifying physical changes which occur at the electrode level and changes in the current collector as critical causes of the end-of-life of cells in a parallel assembly.[17] The internal impedance of cells has also been shown to be impacted by stresses generated in the curvature of electrodes with Mussa et al. highlighting this by comparing samples harvested from curved and flat regions of a prismatic cell after aging.[18]

In a series of studies Arnold et al. found that gradual mechanical deformation while cycling was a major cause of capacity loss and degradation over the lifetime of the cell. They first found that "mechanically induced separator creep" greatly reduced internal cell resistance and increased capacity fade,[19–21] later showing that it could also promote local lithium plating.[22] They later established that the stack pressure within a cell was constantly fluctuating during charge and discharge but also gradually, irreversibly increasing.[23] Much work has been done to better understand both the nature and the effects of the volume change in cells while cycling. These studies have been performed on small bespoke samples,[24] as well as individual cells[25] or even larger battery packs.[26]

In previous studies, the authors found that through non-destructive X-ray computed tomography (CT) the initial heterogeneities within the jelly-roll could be identified. These initial imperfections were shown to act as nucleation points for increasing deformations which further decreases the accessible capacity of the cell.[27] The work here extends the previous study by looking at the lifetime of the cell and systematically describing how the initial imperfections grow and continue to manifest, eventually negatively affecting the lifetime performance of the cell. While X-ray CT is traditionally not seen as rapid technique, the authors have shown the ability to acquire scans required for digital disassembly in as little as 80 s,[27] providing a pathway for use of X-ray CT with digital disassembly as quality control for cell manufacturing.

Experimental

Battery cycling.—Experiments were carried out on a single LG M50 21700 cell (INR21700, 5000 mAh, LG Chem Ltd., Seoul, South Korea). This cell contains a mixed SiO_x/graphite anode and a nickel manganese cobalt oxide (NMC) cathode. Battery cycling was performed using a Maccor 4300 (Maccor Inc., Oklahoma, USA) as well as a Bio-Logic SAS BCS-815 (BioLogic Sciences Instruments, Sevssinet-Pariset, France). All testing was conducted within the manufacturer's operating limits. The cell was charged and discharged for 1145 cycles at the following conditions. Charging was conducted at 3.5 A (0.7 C) until 4.2 V with the voltage held constant until the current tapered to 119 mA, followed by a 10 min rest. The cell was discharged at 5.0 A (1 C) to 2.5 V followed by a 20 min rest.

[z]E-mail: j.b.robinson@ucl.ac.uk

During the in situ charging experiment the cell was charged at the same rate, but imaged at every 100 mV from 2.9 V until 4.2 V (i.e., 2.9 V, 3.0 V, 3.1 V etc.). The cell was removed from the cycler while being imaged. The discharge capacity vs cycle number for the cell can be seen in Fig. 1.

X-ray computed tomography.—For the durability study, the cell was imaged at intervals of 25, 50 or 100 cycles for the duration of its lifetime. The choice of interval depended on the desired time resolution based on the current status of the cell. The scans were performed on a Nikon XT H 225 X-ray computed tomography instrument (Nikon Metrology, Tring, UK). For a typical scan the instrument was operated at 170–215 kV, with a current of 88–-210 μA. In all cases between ca, 1400–3200 projections were collected, each with a 1 s exposure time. The conditions varied slightly from one scan to another, individual scan details can be found in Table S1 in the Supplementary Information.

The conditions for the in situ charging study are as follows: following each charge step of 100 mV, the cell was imaged twice using a Nikon XT H 225 instrument. The first image encompassed the entire cell and was performed immediately after the cell had finished charging. For the first scan the instrument was operated at a source voltage of 190 kV_p using a W anode for a characteristic X-ray peak at 58 keV (W-Kα) with current of 165 μA, projected in a cone-beam geometry through a 0.55 mm copper filter. Between 1900 and 2000 projections were recorded with a 500 ms exposure time, recorded through 360 degrees of sample rotation. The second scan was performed immediately after the first scan and encompassed a magnified region of interest through the diameter of the entire cell. For the second scan the instrument was again operated at a source voltage of 190 kV_p and a W anode but with a current of 100 μA and again with a 0.55 mm copper filter. A total of 2300 projections were recorded with a 500 ms exposure time, recorded through 360 degrees of sample rotation.

The X-ray radiograph images were reconstructed using commercial reconstruction software (CT Pro 3D, Nikon Metrology). The lifetime durability scans as well as the first scan taken in the in situ study had 39 μm isotropic voxels. The region of interest scans resulted in 15 μm voxels.

Digital disassembly.—Digital disassembly is a non-destructive X-ray CT technique which extracts important structural information from the cell by extracting contours from the jelly roll.[27] These contours are made up of the repeated layers within the electrode assembly. In this case the contour is formed at the boundary of the separator and the cathode. The separator and anode very lowly attenuate and appear very dark in greyscale reconstructions, whereas the cathode very highly attenuates and appears very bright: the high contrast at this boundary makes it ideal for contour finding. This process separates the jelly roll into two distinctive bands; the first thinner band consists of the double layer cathode and current collector and the second thicker layer of the separators, double layer anode and anode current collector. A detailed schematic can be seen in Fig. 2. From here the thinner bands will be referred to as the cathode layers and the thicker bands will be referred to as the anode layers.

Before contour extraction an adaptive edge enhancement algorithm is applied, generally utilizing a small kernel median filter, an unsharp mask and a Gaussian difference. Finally the contour of choice is extracted using a modified marching cubes algorithm around the mean of the image. Jelly roll contours are particularly informative when "unrolled" as seen in Fig. 2b. To unroll the jelly roll, a simple coordinate system transform is performed on the extracted jelly roll. Specifically the Cartesian coordinates of the contour are transformed into cylindrical coordinates according to:

$$r = \sqrt{(x - x_0)^2 + (y - y_0)^2} \quad [1]$$

$$\phi = \arctan\left(\frac{y - y_0}{x - x_0}\right) \quad [2]$$

Where x_0 and y_0 are the x and y coordinates of the centre of the cell respectively. Presenting the transformed data is helpful for identifying initial imperfections in the jelly roll structure and tracking how they progress over time into large deformations.

Strain mapping.—Strain mapping refers to tracking how individual sections of the electrode deform over time. Here strain refers to

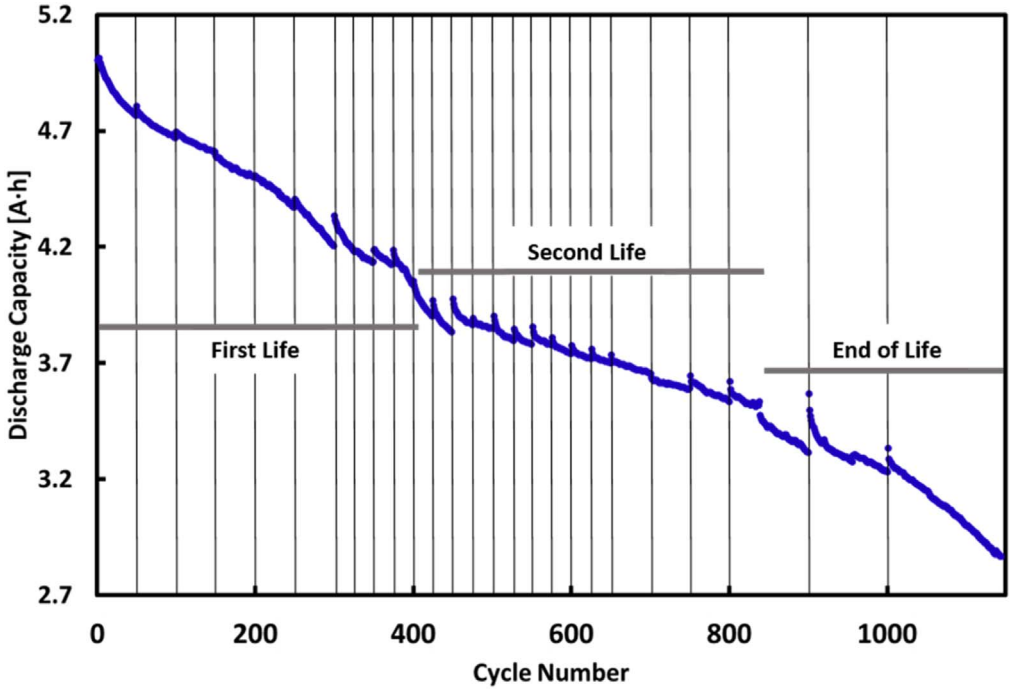

Figure 1. Discharge capacity vs cycle number. The periods representing the cells first life, second life and end of life are indicated on the figure. The jagged appearance is due to the cell being removed from the cycler and recovering some capacity.

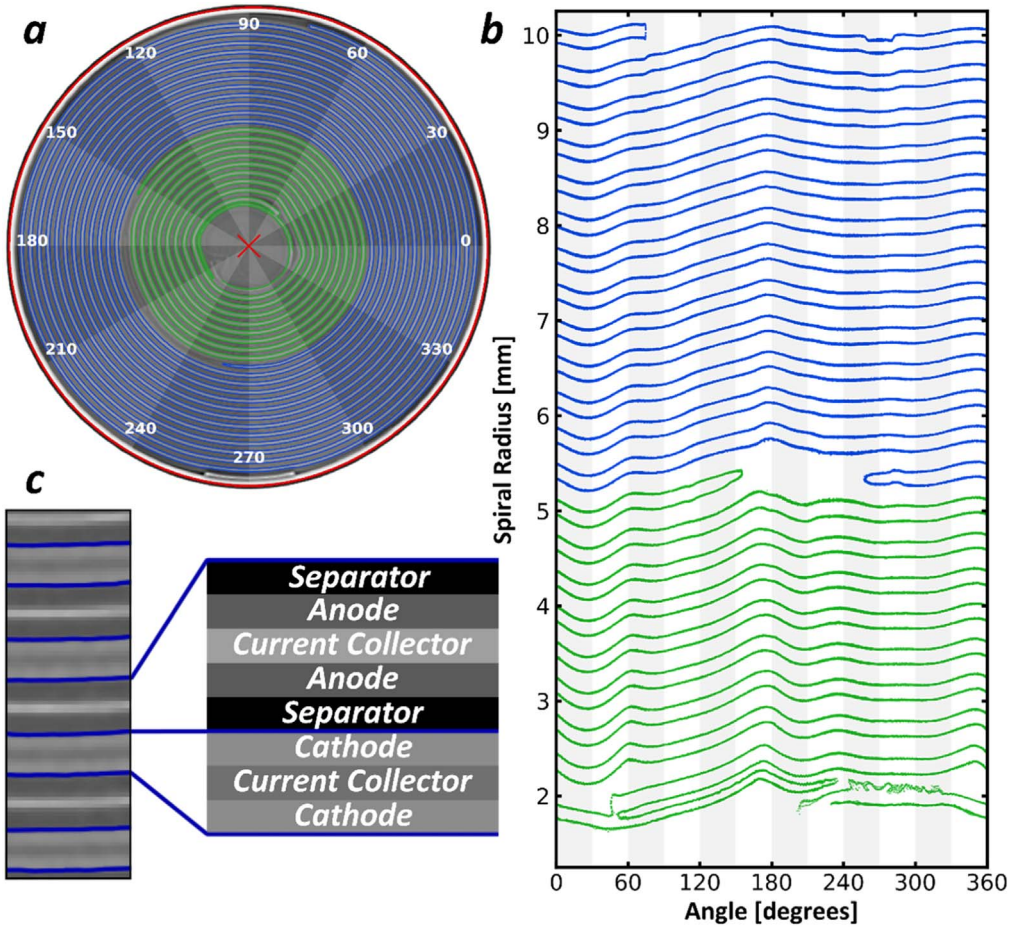

Figure 2. (a) An orthoslice of the 3D tomogram of a Li-ion cell. The lines represent the contours extracted during the unrolling process. There are two distinct jelly-rolls extracted here, the inner jelly-roll in green and the outer in blue. The centre of the cell, represented by the red "X" is found by minimizing the eccentricity of the cell casing, in red. (b) The unrolled jelly-roll. A coordinate system transform around the centre of the cell allows the contours to be represented with a rotation angle and radius. The unrolled view only explicitly shows the cathode layers, while the anode layers are implied by the space between the repeating structure (c) A schematic detailing the repeated structure confined within the contours.

displacement vs an earlier scan. Strain distributions qualitatively show where and how severely the jelly roll has deformed. An example of a strain distribution is presented in Fig. 3a, here arrows are drawn at every integer angle from 0–360° and at every winding of the jelly-roll. The arrows indicate the magnitude and direction of the local electrode deformation (blue arrows indicate inward deformation and red indicate outward deformation).

Results and Discussion

The cell was cycled 1145 times and imaged with X-ray CT at intervals of 25, 50 or 100 cycles throughout its lifetime. The length of the interval depended largely on the time resolution of the data that we suspected would be relevant by continuously monitoring changes in cell capacity. In total the cell was scanned 25 times, one pristine scan and 24 scans while cycling. In addition, after 300 cycles in situ scans were performed on the cell while it was being charged. The change in discharge capacity over the lifetime of the cell is shown in Fig. 1. The degradation observed in the M50 cell used in this work can be seen to be relatively linear, similar to that observed by Ecker et al.[28] and Harlow et al.[29] although it should be noted that the in this work rate of degradation is more similar to that observed by Ecker et al. There are a number of factors which may contribute to this including the absolute current used, in this instance higher, which will result in higher thermally induced stresses manifesting in the electrodes. Interestingly the faster degradation cycles observed in both this work and that of Ecker et al. were obtained using a cylindrical geometry. In contrast, the outstanding performance shown by Harlow et al. (>4000 cycles at 20 °C) was demonstrated in a pouch cell format, in which the deleterious impact of electrode expansion and stress generation is mitigated to a significant extent by the flexible housing of the cell. In this work the transition between the first and second life is defined as the point at which 80% of the initial capacity is retained upon charging (here 4.16 Ah) with the transition between second and end-of-life being the point at which a further sharp change in retained capacity is observed. In this instance this second transition point corresponds to approximately 70% of the original capacity (3.64 Ah); these points are indicated in Fig. 1.

While the capacity curve may appear relatively flat overall, between the first and second life the slope significantly increases. Similarly the end of life begins with a sharp downturn in the capacity curve. The capacity curve shows discontinuities as a result of the cell being removed from cycling to facilitate the XCT scanning. When the cell is removed from the cycler for a period of time it temporarily recovers some capacity likely as a result of the equalization of the concentration gradient in both the active material and electrolyte, this intermittent pausing for small durations (⩽2 h) has been shown to not impact the degradation rate of cells. Generally on returning to cycling the cell quickly loses the regained capacity and returns to its pre-scan capacity. One very significant recovery at 300 cycles was due to the in situ charge study presented later. Another similar feature can be seen at 900 cycles, when the cell was removed from the cycler for Holiday shutdown. Here the cell's life is analysed looking at its first life, second life and finally its end of life as indicated in Fig. 1.

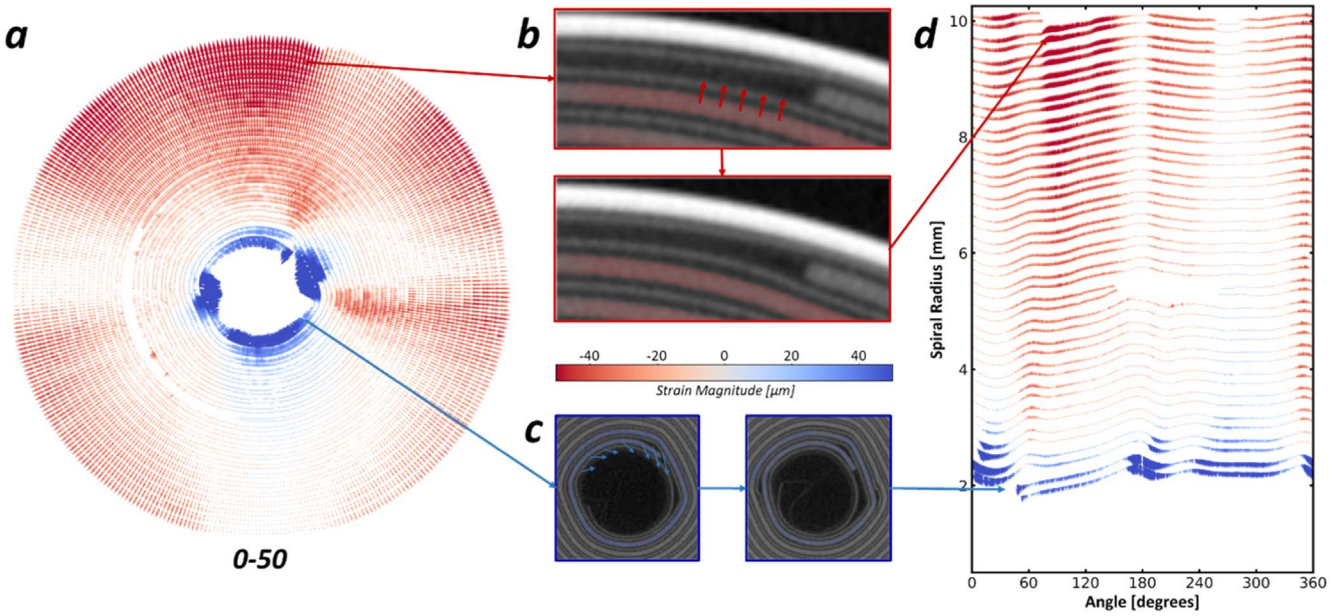

Figure 3. (a) Strain distribution between zero and 50 cycles in the rolled configuration. (b) Subsection of the greyscale orthoslice detailing how the outer areas of the electrode expand to fill into any available space. Here the electrode can be seen in its pristine condition (top) followed by its position after 50 cycles (bottom). The electrode deforms into the space left by the end of the jelly-roll. (c) Left to right shows the centre of the pristine jelly-roll vs the jelly roll after 50 cycles. The jelly roll has unwound slightly, generally moving clockwise and inward. (d) Strain distribution between zero and 50 cycles in the unrolled configuration.

First life (cycle 0–404).—The first life of a lithium-ion cell is generally recognized to last until the cell retains 80% of its initial capacity: for the cell studied here, the first life lasted 404 cycles, this is shorter than the expected manufacturers cycle life (500 cycles at 0.3 C charge, 0.2 C discharge) however the cycling protocols used were more aggressive than this (0.7 C charge and 1 C discharge) although these remained within the manufacturers recommended cycling limits for the cell. Over this time the jelly roll experienced significant degradation. To analyse how and why the cell degraded we first examine the pristine uncycled cell, as received from the manufacturer. An example of the uncycled cell in the unrolled configuration can be seen in Fig. 2. Previous studies have shown that imperfections in the pristine jelly roll form nucleation points for future, much more significant deformation. There are two such imperfections visible in this cell: the first is centred at approximately 30° and the second diametrically opposite at ca. 210°. As the cell is cycled, the electrodes expand and contract, exerting significant stress on the jelly roll. The jelly-roll deforms under this stress, and these deformations can affect the performance of the cell, by promoting particle cracking, electrode delamination and other destructive events.

During formation the focus of manufacturers is on ensuring reliable electrochemical performance over the stated lifetime of the cell by forming a stable SEI, with little consideration given to equalising radial and hoop stresses within the electrode. As a result of this cells in their pristine state may have electrodes under heterogeneous stress conditions. During the initial cycles the stresses generated during cycling result in the jelly-roll to straining and deforming, which allows it to reorganise into a new, metastable state. In the first 50 cycles, the cell presented here deforms very significantly throughout. Figure 3 shows the strain distributions between zero and 50 cycles. Figure 3a shows the results in the "rolled" configuration while (d) shows the "unrolled" results.

The rolled view shows that the majority of the jelly roll has expanded outwards, while the very inner windings have begun to move inwards, effectively "unrolling" the jelly roll. The stressed electrode expands and fills whatever free space it can. In the outer part of the jelly roll this is the space left by inconsistencies in the outer housing of the cell, specifically where features of the cell's internal architecture causes deviations in the cylindrical path of the wound electrode. There are three locations where this takes place, on either side of the tab (270°) and at the very end of the jelly roll (70°). The inset images in Figs. 3b, 3c shows the effect as seen in the reconstructed volume. At those locations in the unrolled view, we see significant outward deformations that propagate through the jelly roll, in some cases reaching to nearly the centre layer.

When the inner layers of electrodes are placed under stress, they exploit imperfections in the jelly roll for relief, which buckle under pressure, allowing the electrode to expand both laterally and radially. Figure 3d shows that the nucleation points identified in the pristine cell have already expanded into larger deformations, which will be referred to as *"kinks*." A kink deformation allows enough freedom of movement from the adjacent electrode layers that they can effectively separate from one another, unwinding the jelly-roll. The initial effects of this can be seen at the bottom of Fig. 3d where the inner layer of the jelly roll has collapsed in on itself. The final inset shows this affect taking place on the reconstructed volume. While initially this effect is very minor, kink deformations are significant weaknesses in the structural integrity of the jelly-roll and will grow over time.

There are also several regions that are conspicuous for not deforming initially. The tab, observable in the white area located toward the bottom of Fig. 3a and at 270° in Fig. 3d acts as an anchor in the jelly roll. Similarly at 180° the jelly roll has a local maximum that also anchors the outer layers of the jelly roll. These positions, along with the initial imperfections in the inner part of the jelly roll have a substantial effect on how the jelly roll deforms while cycling, and the performance of the cell in general.

Following the initial reorganisation, the jelly-roll reaches a metastable position and the deformation drastically slows. Figures 4a–4c shows the strain distributions for the cycles 100, 150 and 200. There is still minor deformation between cycles 50 and 100. The inner electrode is still unwinding slightly, leading to a net inward deformation in the centre of the jelly-roll. There is also significant strain at the kink deformation, which continues to grow after forming in the initial 50 cycles. Figure 4d shows the position of the pristine jelly-roll vs its position at 200 cycles. Analysing the inner windings of the jelly-roll, from 350° to 30°, shows that the initial nucleation point is now a significant kink deformation that has propagated through the first four layers of the jelly roll.

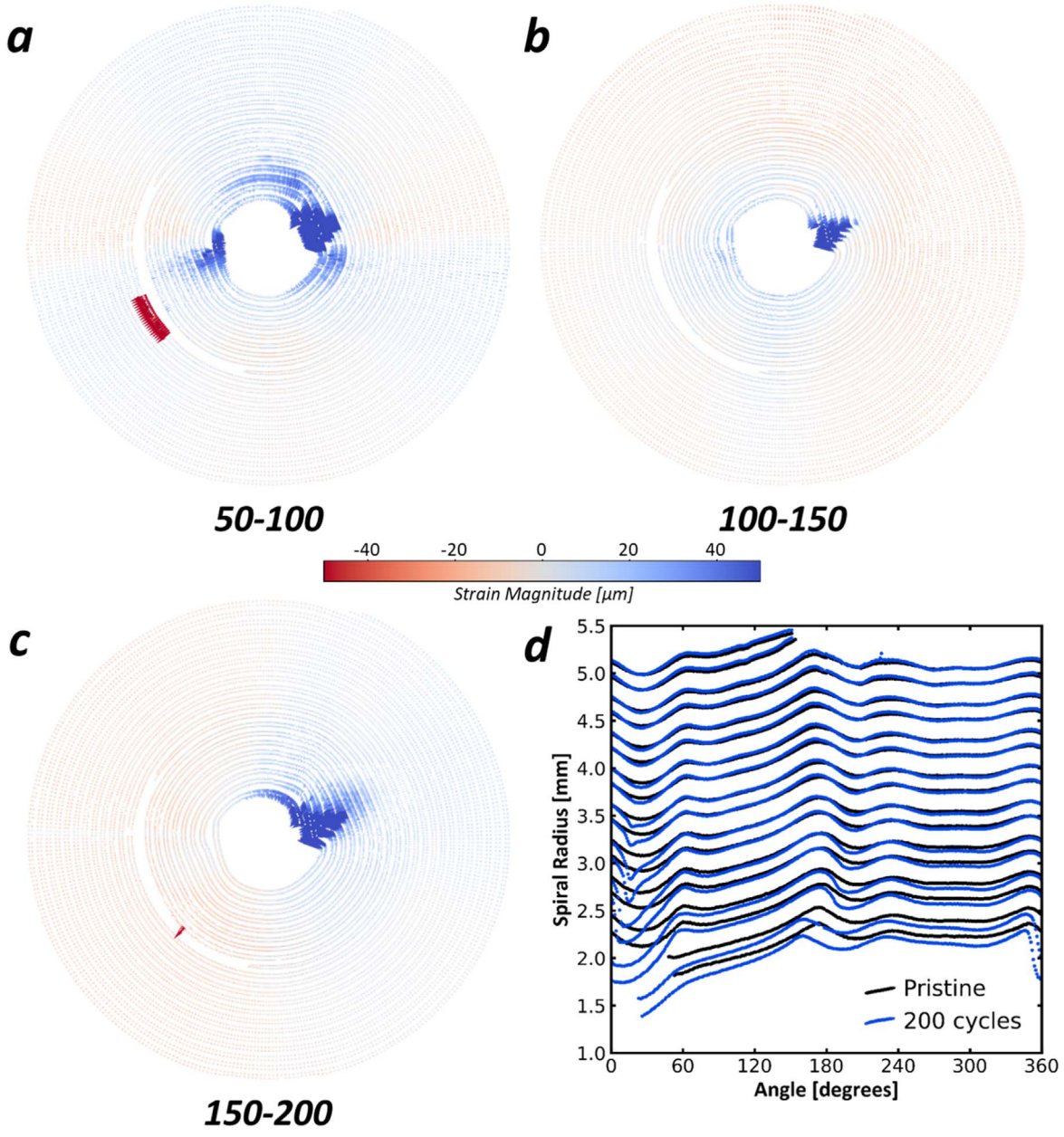

Figure 4. (a) Strain distribution for 50–100 cycles. (b) Strain distribution for 100–150 cycles. (c) Strain distribution for 150–200 cycles. (d) Comparing the unrolled pristine inner jelly-roll (black) with the jelly-roll after 200 cycles (blue). The kink deformation, visible between 0° an 60°, now penetrates through four electrode layers.

Between 200 and 250 cycles the deformation begins to accelerate. The kink deformation penetrates deeply through the inner electrode, affecting the first 11 windings, essentially the entire inner jelly-roll. The structural integrity of a jelly-roll is based mostly on maintaining a radial (outward) stress due to the hoop stress of winding stiff materials around each other. As the kink propagates through the layers, the stabilizing stress is relieved, negatively affecting the structural integrity of the jelly roll and allowing it to collapse in on itself. The beginning of this process can be seen in Fig. 5a which shows the strain mapping between 200 and 250 cycles. Between 250 and 300 cycles [Fig. 5b] the collapse becomes much more drastic, the entire inner jelly-roll separates from the outer jelly-roll. The inner jelly-roll (as defined in Fig. 2b) collapsing off the outer relieves stress in the outer jelly-roll, causing it to expand into the casing in a process similar to the initial "reorganising" in the first 50 cycles.

The inner jelly-roll continues to collapse between 300 and 350 cycles [Fig. 5c]. At this point the collapse has expanded through the entire inner jelly-roll and is beginning to affect the lower layers of the outer jelly roll. Figure 5d shows the average contour gap of each layer in the inner-jelly roll for each of the X-ray CT scans described previously. The gap in the contour is an effective measure of the thickness of the layers each contour represents. On the left is the thinner of the electrode layers, the cathode layers in this case, and on the right the thicker anode layers. It is clear that the anode layer gap widens early in the cycling, and that over time the effect doesn't become more acute, but rather affects a larger portion of the inner jelly-roll. Perhaps the most important feature can be seen in the cathode layers. While there is a general, slow widening in the layers over cycling, there is also a clear step change at 300 cycles. It is very important to note that there are several mechanisms for the gap in the contours to increase or widen. The layers themselves, anode or

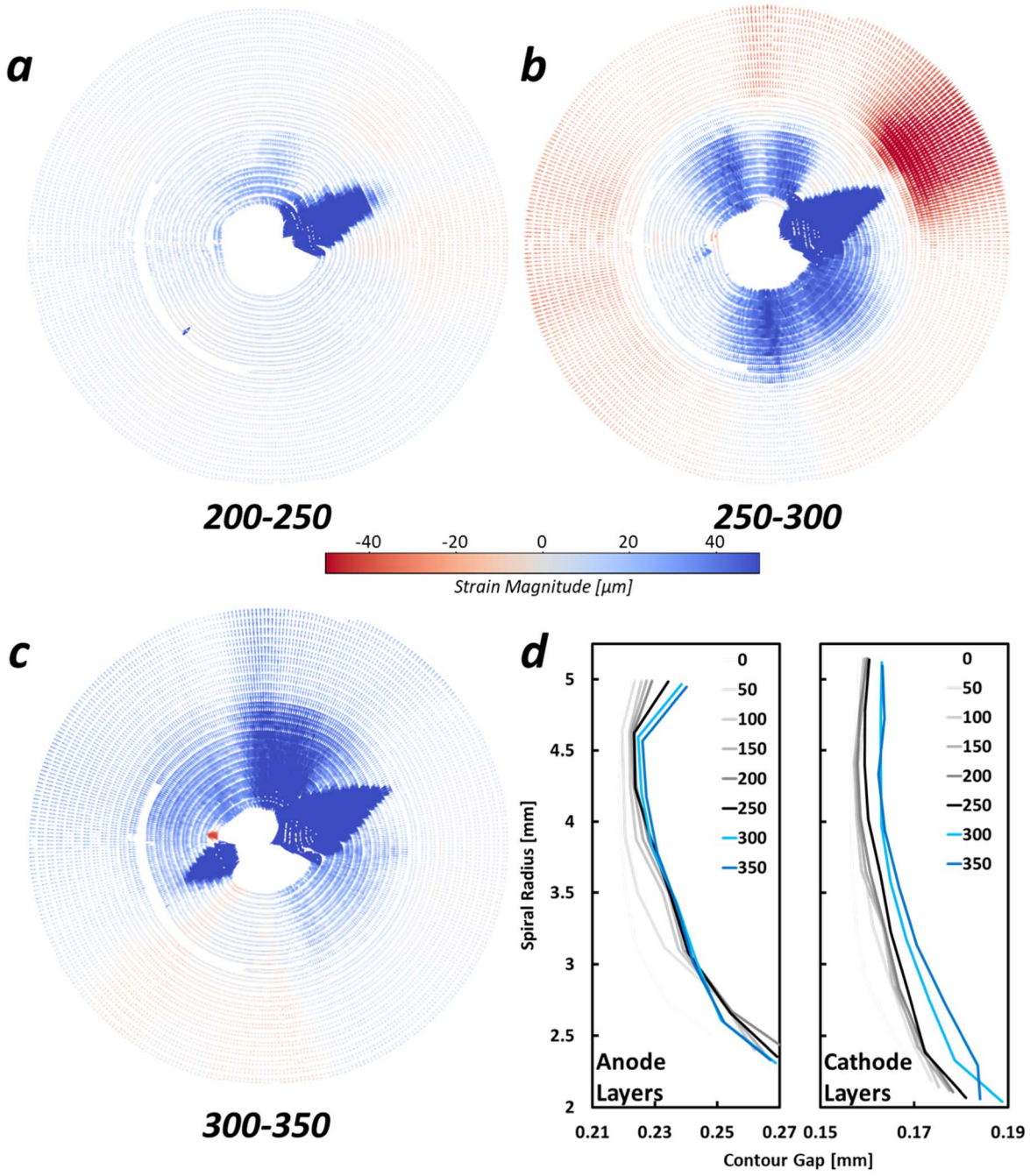

Figure 5. (a) Strain distribution for 200–250 cycles. (b) Strain distribution for 250–300 cycles. (c) Strain distribution for 300–350 cycles. (d) (left) Anode layer contour gap for the inner jelly-roll for different cycles. (right) Cathode layer contour gap for the inner jelly-roll for different cycles. All cycles before 300 are coloured in grey-scale and cycles 300 and 350 in shades of blue to make the distinction between the data sets easier. Note the large step change in cathode contour gap at 300 cycles.

cathodes, could be physically expanding and getting larger (for example due to irreversible expansion of the anode layer) or the contours could be widening as the stress pressing them together is reduced, which would be consistent with the collapsing inner jelly-roll seen in Figs. 5a–5c. In this case, the sudden widening of the cathode contour at 300 cycles should be attributed to the collapsing jelly-roll.

The next scans were done every 25 cycles, to try to capture the dynamics of the collapsing jelly roll with higher fidelity. By 375 cycles [Fig. 6a] the continuing deformation was limited to the initial kink deformation and a new deformation that had more recently developed in the second initial jelly-roll imperfection. Between 375 and 400 and then 400 and 425 cycles [Figs. 6b, 6c] this trend continues. Any additional stresses generated in the jelly roll are offset by the significant freedom of movement afforded by two kink deformations. The jelly-roll has achieved another metastable position.

Until now all discussion has focused solely on the mechanics of the jelly-roll deformation. This has been analysed independently of capacity fade or electrochemical performance. In Fig. 7 the mechanical deformation is compared to the electrochemical performance over the first life of the cell. The strain distributions in Fig. 7 are presented in the unrolled view.

From the strain distributions patterns presented in Fig. 7 it is clear that the structural mechanics of the jelly-roll correlate well with the capacity fade in the cell. Specifically as the inner jelly-roll begins to

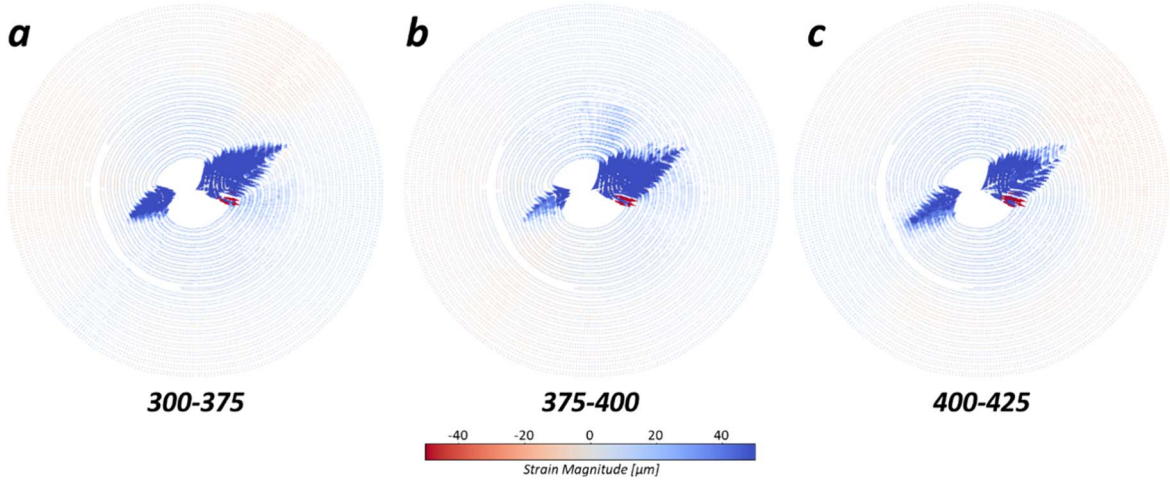

Figure 6. (a)-(c) Strain distributions for cycles, 350–375, 375–400 and 400–425 respectively.

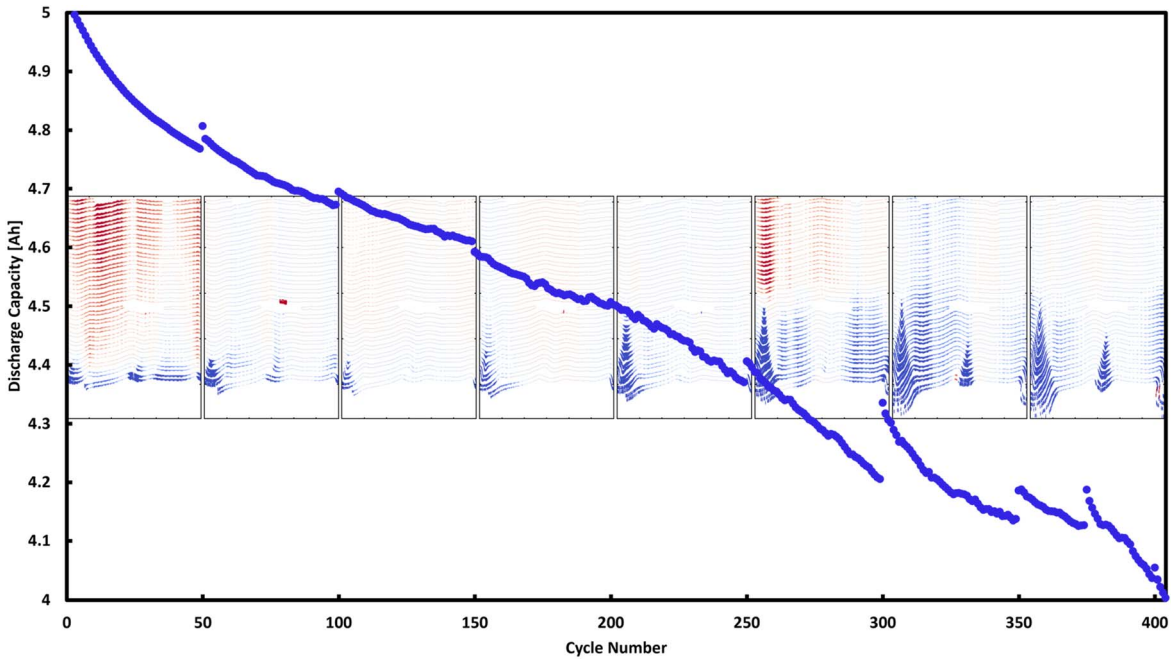

Figure 7. Discharge capacity for the first 400 cycles overlaid with the strain distribution for every 50 cycle segment. The strain mapping is presented in the unrolled view and each distribution physically spans the range of cycles it represents. The capacity is discontinuous at 375 cycles because the cell was taken off and scanned at this point, however the strain distribution shown in this period is for 350–400 cycles. The axis titles for the inset images are the same as in Fig. 1b, namely the angle (degrees) for the *x*-axis and spiral radius (mm) for the *y*-axis.

collapse between 200 and 250 cycles the cell capacity begins to experience what has often been referred to as a "knee-point," or a sharp downturn in retained capacity.[28] As the inner jelly-roll collapses in on itself, the spacing between layers drastically increases, simultaneously decreasing the compressive force maintaining good contact between the layers. This compression is necessary to maintain good electrical contact between the layers, as it decreases the electrochemical pathways are elongated, reducing the efficiency of charge transfer and the accessible capacity. While typically batteries are considered to have reached end-of-life once 80% of the original capacity remains[30] the loss of this compression will result in an increase in the impedance of the cell and will further contribute to the loss of performance in electric vehicles and other high-power applications.

In addition, during this period the kink deformations are rapidly growing. The electrodes in these kinks have been significantly damaged in their as the kinks increase in magnitude. Figure 8 shows a progression of orthoslices from a tomogram taken at 375 cycles at increasing resolution. Figure 8a shows the YZ orthoslice, showing the side view of how far the kink deformation has expanded through height of the cell with Fig. 8b showing in the middle is an orthoslice showing the macro view of the kink and Fig. 8c showing is a detailed region of interest scan of the main kink deformation. In this final view the delamination and general damage done to the electrode can be seen.

In situ charging.—After 300 cycles had been completed, complementary in situ X-ray CT images of the cell were taken while charging. The cell was imaged at 2.5 V, 2.9 V and then at 100 mV increments until 4.2 V. In between the scans the cell was returned to the cycler. At each voltage the cell was imaged twice, once at the normal resolution and then a following scan ca. 20 min

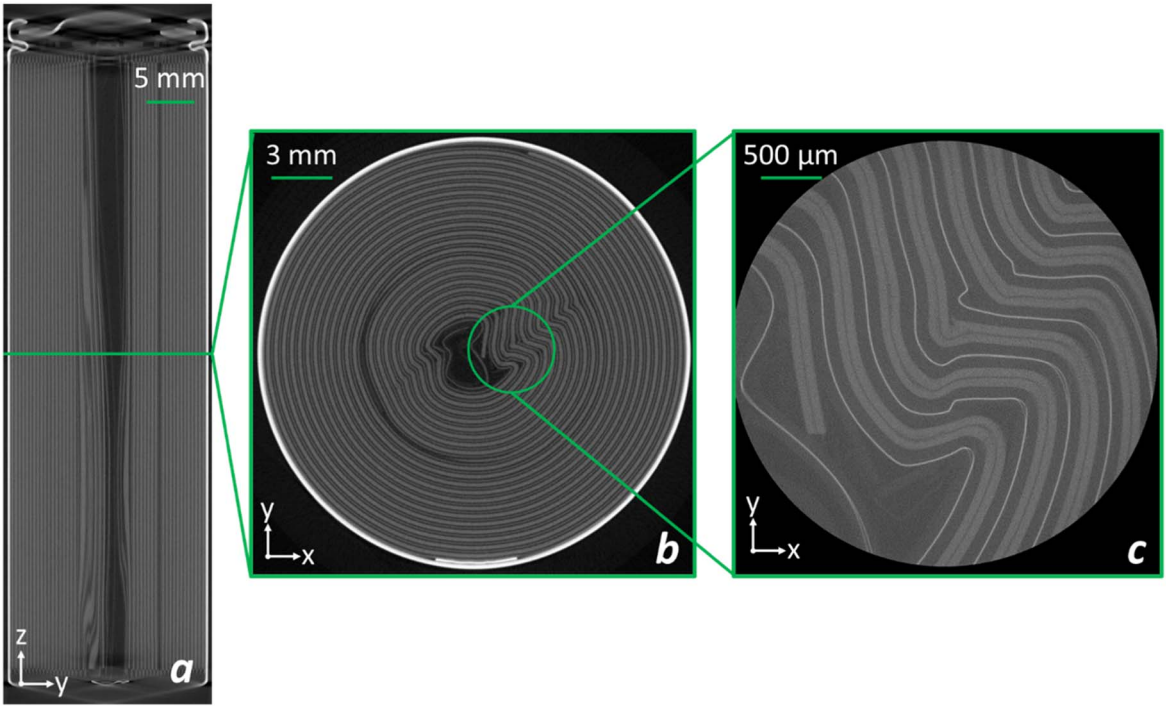

Figure 8. (a) YZ orthoslice showing the interior of the cell at 375 cycles. Of note is the height of the kink deformation, It extends through more than half of the electrodes total height. (b) XY orthoslice of the same cell. (c) XY orthoslice of a high resolution region of interest scan of the cell in the same state.

later at a higher resolution. This aspect of the study was undertaken to better understand the mechanisms behind deformation in the jelly-roll with higher time resolution over a shorter time-scale.

The image in Fig. 9a shows the unrolled image of the cell at 2.5 V but with the space between the contours coloured according to the size of the gap. It is immediately clear that the spacing of the contours is not consistent throughout, but subject to significant variability. The remaining plots in Fig. 9 describe how the gaps between contours change while the cell is being charged. Figure 9b shows how the average contour spacing for the anode layers and the cathode layers varies during charging. As would be expected due to the irreversible anode expansion which can occur on cycling there is an overall increase in size of the anode layers while charging and a corresponding decrease in the cathode layers. Importantly, very little variation takes place in either the anode or the cathode layers before 3.5 V, with the majority taking place after 3.6 V. This follows the charge transfer profile, with the onset of the charge transfer in the bulk of the material taking place after 3.5 V, suggesting the majority

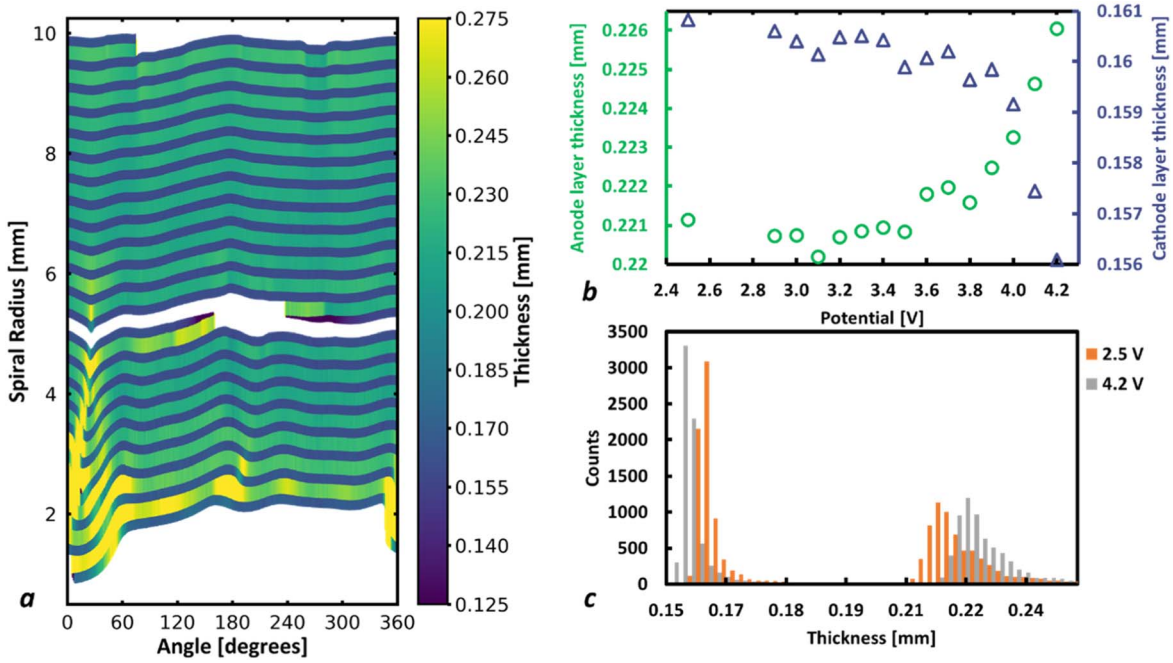

Figure 9. (a) The unrolled jelly-roll at 2.5 V with the contours filled in according to the local contour spacing. (b) The average contour spacing of the anode layers (green) and the cathode layers (blue) as a function of the cell potential during the charging process. (c) Histograms of the contour spacing at 2.5 V (orange) and 4.2 V (grey). The tighter peaks on the left of the plot are the cathode layers and the broader peak on the right is the anode layers.

of the expansion in the anode is due to lithium intercalation. A differential capacity plot of is available in the supplemental information. Figure 9c shows the histogram of contour spacing for the cell at 2.5 V (orange) and then the final distribution at 4.2 V (grey). The narrow distributions on the left of the plot represent the cathode layers and the wider distribution on the right show the anode layers. There is far more variability in the anode contours than the cathode contours, however in both cases the shape of the distribution remains constant between 2.5 and 4.2 V, suggesting uniform change throughout. The data points represented in Fig. 9b are averages over ca. 50000 distinct measurements. As such the standard error associated with these measurements is less than 0.1 μm.

Figure 10 details how the contours representing the anode layers change while the cell is being charged. The plots on the left and in the centre show the inner and outer jelly-roll anode layers respectively. The figure on the right is provided for reference, detailing the naming scheme of the layers. Every anode layer excluding \the innermost (A21) expands monotonically after 3.6 V until the charging has completed at 4.2 V. The equal and near constant expansion with cell potential provides more evidence that the underlying mechanism is the intercalation of lithium ions into the graphite-Si anode, causing it to expand.

The variation in the anode spacing evident in Fig. 9c is shown in more detail here. The anode layers located in the outer jelly-roll are similar in spacing, with all the layers appearing between 220 and 240 μm while in the inner jelly-roll some the contour spacing ranges from 220 to 270 μm. This is consistent with the analysis presented in the first part of this work. When the in situ charging study took place, at 300 cycles, the cell was mid-way through a "collapsing event" characterised by the inner jelly-roll rapidly deforming inward as the cell loses structural integrity.

The dilation of electrodes during lithiation leads to unbalanced forces and residual stresses within the jelly roll assembly. Previous work has postulated that these unchecked forces eventually lead to large buckling deformations in the jelly roll.[27] To better understand the heterogeneous nature of the jelly-roll deformation during charging, we analyse how the jelly-roll is deforming relative to the beginning of charging. Figure 11 shows the strain distributions for 2.9 V, 3.6 V and 4.2 V relative to 2.5 V. The first row of images, Fig. 11a, shows the strain distribution for the scans taken immediately after removing the cell from the battery cycler. At 2.9 V the jelly-roll had not noticeably changed from its initial state. By the time the cell had reached 3.6 V, significant heterogeneous deformation in the jelly roll can already be seen. There are two areas of significant inward (blue) movement. The first is the large kink deformation on the right side of the innermost part of the jelly-roll. The inward movement of the kink is expected. The kink is a failure mode that resulted from insufficient space for the strained electrode to expand into, unsurprisingly adding further force causes the electrode to expand into this newly free space. The second region of inward movement spans the majority of the top hemisphere of the cell.

By 4.2 V both major deformations are still present and have become more intense. Interestingly similar, but smaller deviations can be seen to have formed opposite the major deformations, likely as a result of increased stress being generated by the larger deformations. Across from the kink deformation a small amount of inward moved is flanked on either side by small outward (red) movement. This feature is the formation of another kink deformation that will appear after further cycling and is discussed later. Most importantly this shows how initial imperfections in the jelly roll are exacerbated and eventually buckle and break under strain, damaging the cell.

Further imaging was performed at each step after a short rest (approx. 20 min). The deformation patterns for 2.9 V, 3.6 V and 4.2 V are presented in Fig. 11b. The strain distributions are very similar in the inner jelly-roll, but noticeably different in the outer regions. Rather than the upper hemisphere deforming inward, as was the case for the initial scans, the entire outer jelly-roll expands outward, contrasting the strain in the inner jelly-roll.

In Fig. 11c the difference between the first (a) and the second (b) scan is plotted. In this case there does not appear to be a progression, or any dependence on voltage. At each voltage the difference appears to be equivalent indicating relaxation of the stressed electrodes.[31,32] Most significantly the large bucking deformation retracts outwardly, and the outer region of the jelly roll generally relaxes back towards the centre of the cell.

While being charged, the electrodes are under significant stress. In the first place, the stress manifests itself as predictable deformations in the jelly-roll, forming around pre-existing nucleation points and other imperfections in the jelly roll. Upon resting the jelly-roll relaxes, reducing the magnitude of the more significant

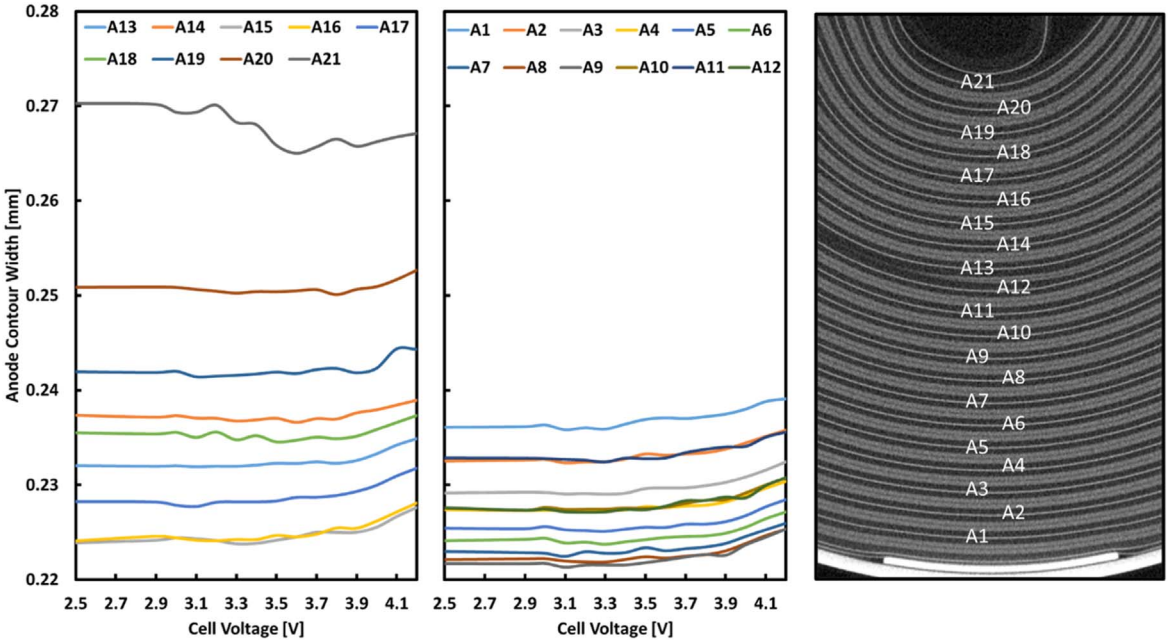

Figure 10. Contour width for the inner (left) and outer (centre) jelly-roll layers. The individual layers are labelled with A1 being the outermost layer and A21 being the innermost layer. The image on the right is provided for reference.

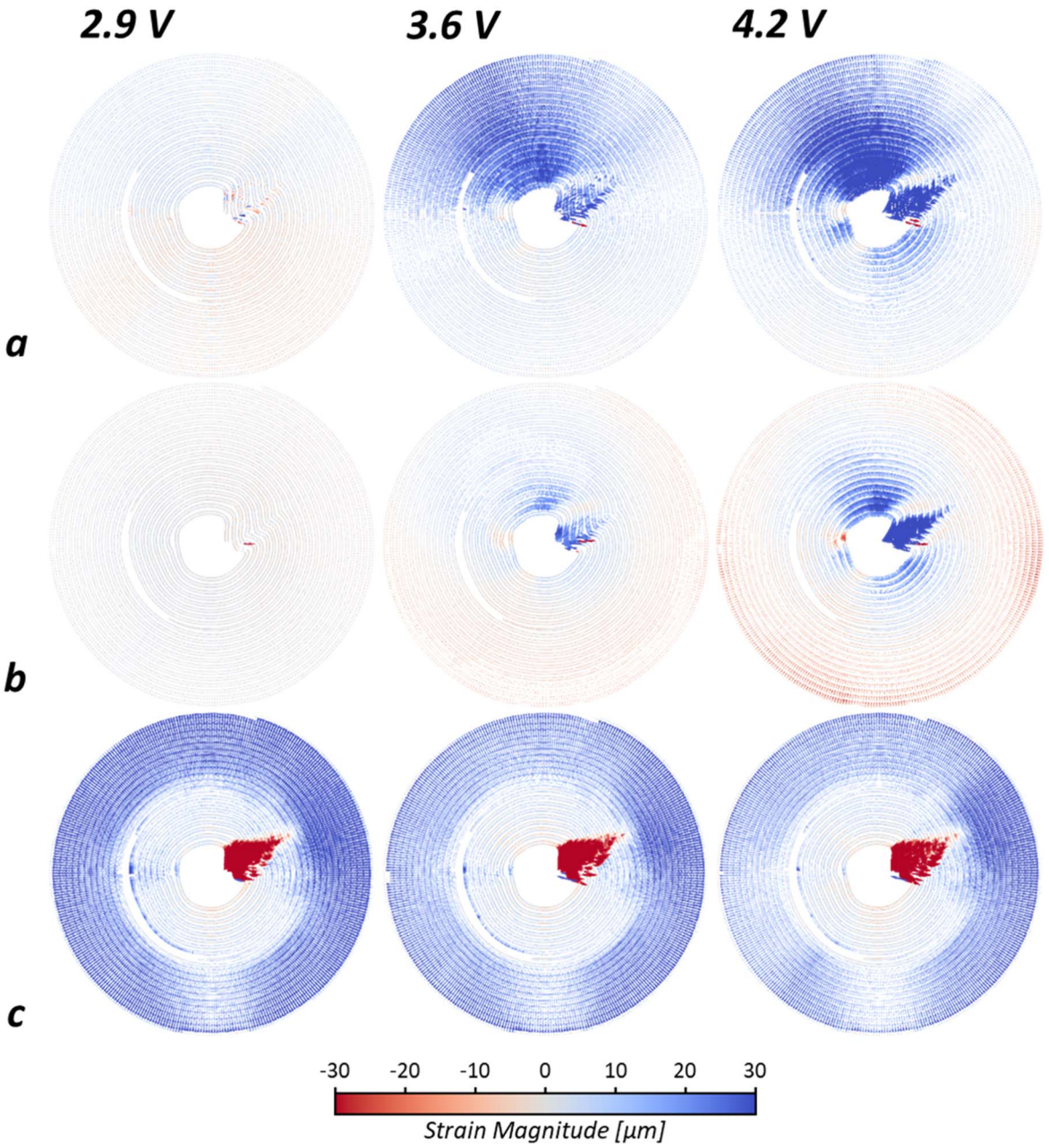

Figure 11. Strain distributions for the jelly-roll deformation during charging. Positive (red) vectors indicate radially outward deformations while negative (blue) deformations indicate inward deformations. (a) The strain maps relative to 2.5 V immediately after the cell had been removed from the cycler. (b) The strain maps relative to 2.5 V from the second scan, after the cell had been allowed to rest for ca. 20 min. (c) The strain maps between the two scans for each potential presented in a and b.

deformations.[33] This constant stress will, over application of hundreds of cycles, lead to the formation of cracks, breaks and buckles in the jelly-roll, reducing its effectiveness as an energy storage medium. Understanding the effect of cycling on the internal structure of the cell is key in developing more robust, longer lasting batteries in the future. Design and manufacture optimisations could be used to mitigate or significantly reduce the impact of heterogeneous deformations in the jelly roll in high-power or mission critical applications.

Second life (cycle 405–838).—The second life of a cell is not as rigidly defined as the first life. Generally it refers to a secondary usage for the cell after its first life has elapsed and before it is no longer useable. Here the second life will refer to the period of time after the first life has elapsed (20% capacity fade @ 404 cycles) and before some other significant degradation event triggers its end of life. As discussed previously while this cycle life is shorter than the 500 cycles outlined by the manufacturer the current ranges are all within the manufacturers recommended limits. In this case the end of life was said to begin at 838 cycles, as the cell capacity has a significant discontinuity at this point, after which degradation accelerates.

The initial period of the cell's second life saw more jelly roll deformation. While the first life of a cell ends at 80% capacity, the largescale deformation and degradation responsible for it continued until a new metastable state was established at ca. 500 cycles, with the capacity fade levelling off at ca. 450 cycles.

Figure 12 shows the strain distributions for cycles 400–425, 425–450 and 450–500. The residual deformation after the major event in the first life is still evident as the kink deformations continue

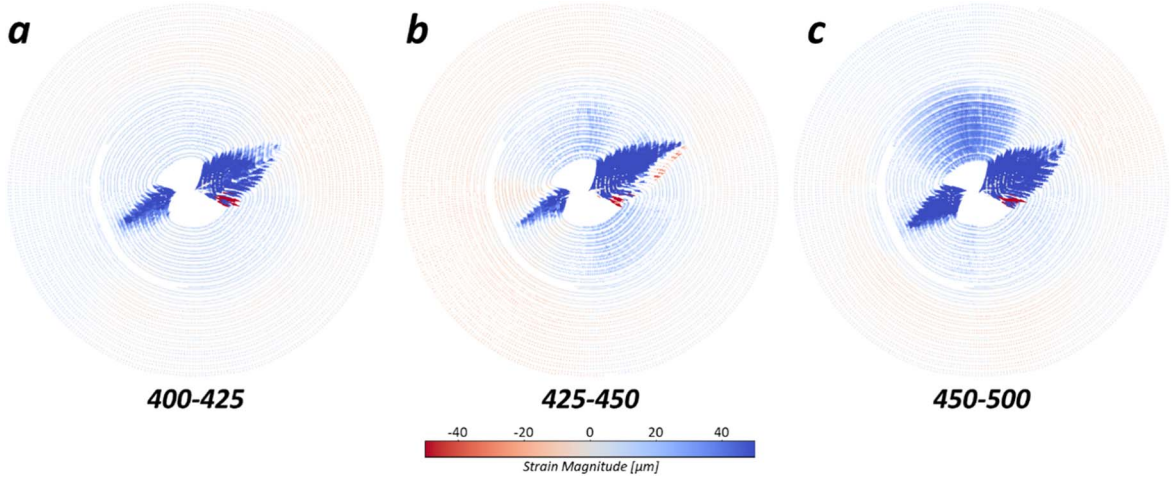

Figure 12. (a)–(c) Strain distributions for cycles (a) 400–425, (b) 425–450 and (c) 450–500 respectively.

to collapse inward. Between 450 and 500 cycles there is significant inward movement perpendicular to the kink deformations, although it doesn't progress beyond that into a large deformation.

Between 500 and 838 cycles very little physical degradation takes place. Over this period the cells capacity drops from approximately 77% to 70%, however it does so very linearly and without the impact of noticeable physical deformation. As mentioned previously during this period the jelly roll is metastable. Figure 13 shows a selection of strain mappings from this period of cycling. Very clearly there is little or no deformation in the jelly-roll, and the collapse present in the inner jelly-roll and the first life has stopped. The remaining distributions can be found in the supplemental information.

End of life (cycle 838–1000).—The cell's end of life follows a very similar pattern to the end of its first life. The sudden change in capacity fade can be correlated to a physical change taking place in the jelly-roll. In this case however the change is very minor, and not directly evident when analysing strain maps for cycles in that period. In Fig. 14 the strain distributions for the periods between 800–900 cycles, 900–1000 cycles and 1000–1145 cycles are presented. While they show more deformation than was present during the stable second life, the deformation they show is very minor and almost negligible compared to the inner jelly-roll collapse and kink formations during the cell's first life.

To correlate the performance decrease with physical phenomena we again look at the anode contour spacing, this time throughout the cycle life of the cell. Figure 15 shows the average anode contour spacing against cycles for the lifetime of the cell. Figure 15a shows the anode layers for the inner jelly-roll and Fig. 15b the outer jelly-roll. The layers are numbered with decreasing radius, meaning A1 is the outermost layer and A21 is the innermost layer.

Starting in the inner jelly-roll we see immediate widening of the contours in the innermost four layers (A21-A18). This is consistent with the jelly-roll "reorganising" reported in Fig. 3. The first two (A21 and A20) peak after 200 cycles, and decrease for the remaining 800 cycles. The next two (A19 and A18) peak around the same time, then continue to increase at approximately the same rate the first two decrease at. In summary, the first four layers rapidly expand and change until 200 cycles, before reaching some form of equilibrium with each other.

After ca. 50 cycles (ca. 850 total cycles) the fifth, sixth and seventh layers (A17-A15) all begin to widen slowly. This is consistent with what is seen in Figs. 4a–4c. Unlike the innermost four layers the change is very gradual, and continues relatively consistently for the entire lifetime of the cell. The most interesting layers are the two outermost, A14 and A15. A14 is the outermost full layer of the inner jelly-roll and A15 is the space between the inner and outer jelly-rolls. In both cases the contours initially widen slightly in their first 200 cycles before rapidly expanding for the next 400 cycles. As they represent the outside of the inner jelly-roll, the collapse of the inner jelly-roll culminates with these layers separating from the outer jelly-roll, in turn, losing a constraining force. This results in significant expansion in the layer, as seen in Figs. 5a

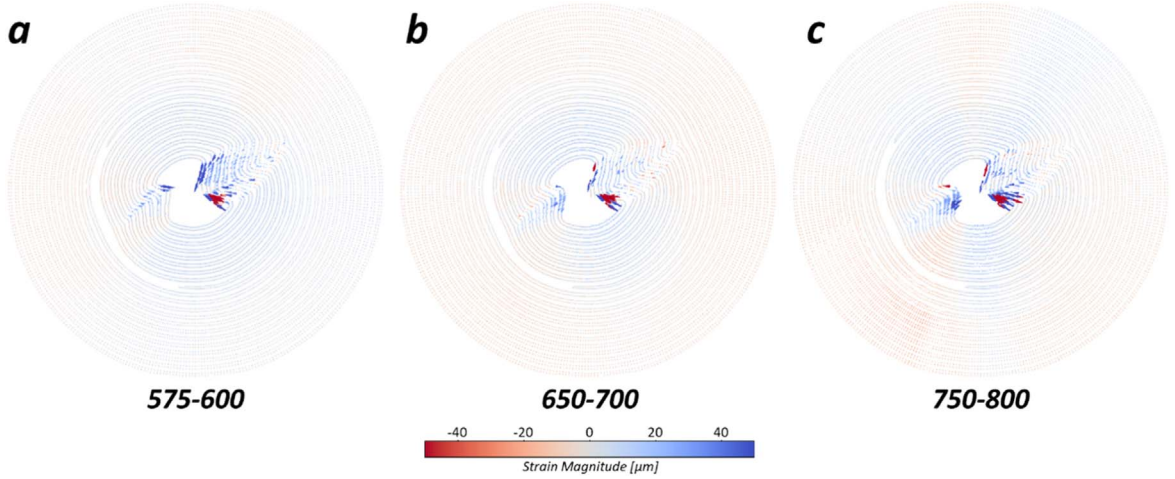

Figure 13. (a)–(c) Strain distributions for cycles (a) 575–600, (b) 650–700 and (c) 750–800 respectively.

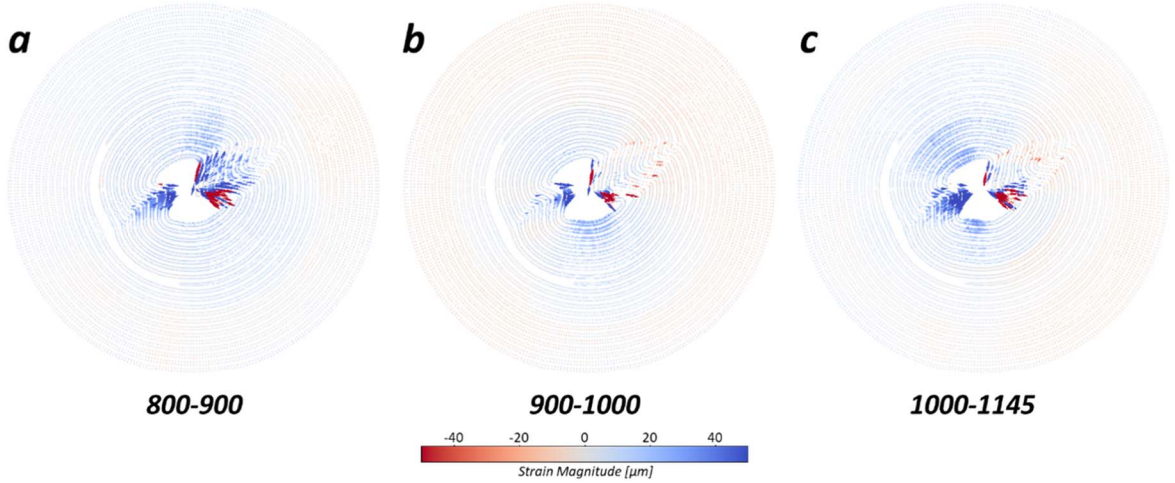

Figure 14. (a)–(c) Strain distributions for cycles (a) 800–900, (b) 900–1000 and (c) 1000–1145 respectively.

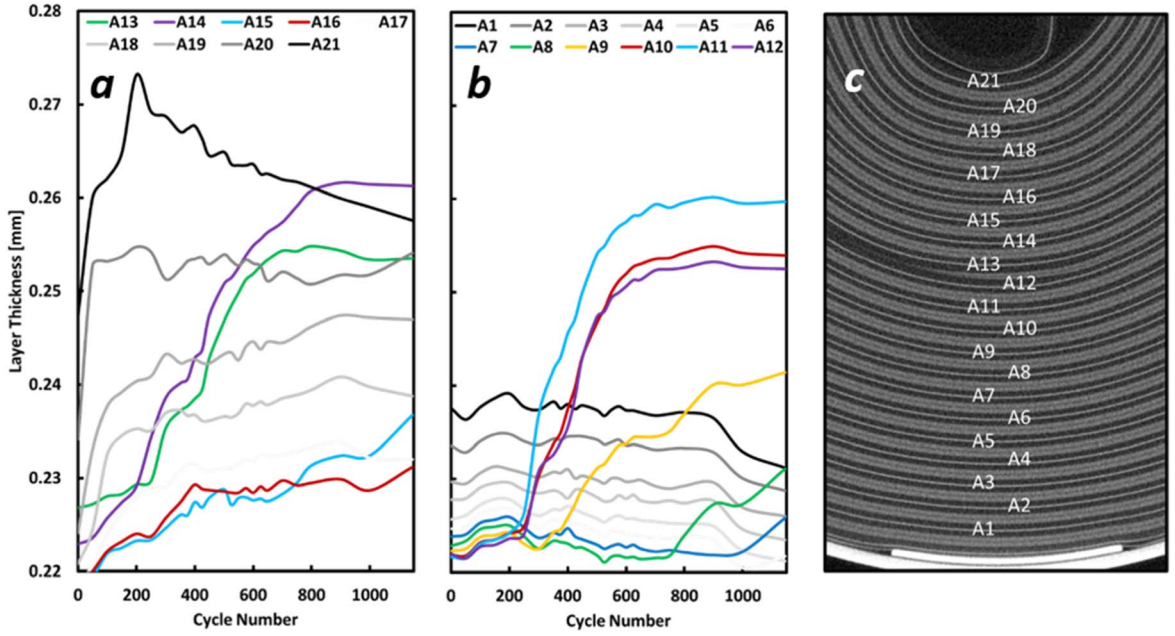

Figure 15. Anode contour spacing for (a) inner jelly-roll and (b) outer jelly-roll. The layers are labelled with decreasing radius. A20 is the most inner layer and A1 is the most outer layer. The layers of interest (outermost layers and inner jelly-roll and vice-versa) are shown in colour while the others are in greyscale. This is simply to make the plot more readable.

–5c. Following this, these layers continue to expand throughout the life of the cell, only appearing to stabilize at around 800 cycles, near the end of the cell's second life. The layers are able to continue to expand through the second life due to the presence of the kink deformations in the inner jelly-roll. Any excess stress produced in the cell can be released through the kink expanding slightly, which will in turn cause the inner jelly-roll to collapse slightly further on itself. This effect can be seen after the major collapse in Figs. 6 and 12, which show the kink deformations expanding despite no obvious effect on the cell's performance.

In the outer jelly-roll (Fig. 15b) the innermost three layers, A12-A10, follow the trend of A13 and A14 very closely. They show very little variation initially followed by rapid expansion at 200 cycles. They also eventually stabilize, but slightly sooner than the neighbouring inner jelly-roll layers. By approximately 600 cycles, the three innermost layers have stopped changing. This is attributed to there being no kink deformation in the outer jelly-roll, making it inherently more stable and resistant to change.

Finally the cause of the end of life can be seen in A9, the next most outer layer. A9 is stable until approximately 300 cycles at which point the larger kink deformation has expanded sufficiently to penetrate through multiple layers of the outer jelly-roll. At this point the layer begins expanding rapidly. The exact mechanism for this expansion is unclear, although it is likely in response to every layer inward of A9 deforming and collapsing into the centre of the cell. The expansion stops at 600 cycles and once again A9 becomes stable for a period. At 750 cycles expansion begins, and this time it has a cascading effect and causes the next outward layer A8 to follow after 800 cycles and finally A7 after the 1000 cycle mark. As was the case with the inner jelly-roll, when the layers of the outer jelly-roll begin to collapse off each other, the capacity fade of the cell increases, in this case triggering the end of life.

Conclusions

A lifetime X-ray computed tomography study was performed on a commercial 21700 lithium-ion cell. The cell was imaged in its pristine uncycled condition and then 23 times at different intervals, normally every 25 or 50 cycles until it had reached 1000 cycles and the end of its life. For each tomogram the contour between the anode and cathode double layers was rigorously extracted through a process called digital disassembly. Upon digital disassembly, the pristine uncycled jelly-roll revealed two imperfections that were predicted to be nucleation points for eventual kink deformations and failure events. These defects arise from the fact that as manufactured cells are wound in an archimedian spiral rather than a pure circle and are commonly observed in cylindrical cells. We hypothesise that the deviations from circularity form an in built lifetime for the cell with high quality manufacturing enabling longer cell lifetimes.

Digital disassembly also allows the strain of the individual electrodes to be tracked as the cell is cycled. Strain mapping revealed that during initial cycles the jelly-roll "reorganises" and finds a new favourable state. The semi-stable period identified following this reorganization was seen to be maintained despite a kink deformation forming out of the larger of the two initial deformations in the pristine jelly-roll which grew until a point at which it triggered the collapse of the jelly-roll. This collapse caused the cell capacity fade to rapidly increase, effectively ending the first life of the cell which had dropped below 80% of its initial capacity resulting in it being reclassified as a second life cell. Between approximately 450 and 800 cycles the capacity fade of the cell stabilized with the jelly-roll was no longer collapsing despite kink deformation growth and nucleation. This period of stability ended when the kink deformation caused the outer jelly-roll to begin to collapse, with two layers beginning delaminate, further reducing the capacity of the cell and triggering its end of life.

Complimentary tomograms of the cell were also taken of the cell charging after it had been cycled 300 times. In this case 30 more scans were taken, two at different resolutions every 100 mV during the charging process. This study provided an insight into the nature of the stress and strain generated during a charge cycle. The results showed that during any individual cycle the jelly-roll changes significantly. This was attributed to the stress caused by lithiation of the anode. The expanding anode has very little room to expand into, causing the jelly roll to exploit any weaknesses in its internal structure to relieve the stress. This study also showed the jelly-roll relaxes significantly when allowed to rest.

This lifetime X-ray CT study has provided significant insights into the degradation mechanics of a cylindrical lithium ion cell. Underlying manufacturing imperfections have been shown to lead to capacity fade and eventual failure. By tracking the shape and structural integrity of the jelly-roll a meaningful understanding of the transmission between first life, second life and eventually end of life has been demonstrated. These results have far-reaching commercial implications, specifically to cell manufacturing. The impact even small imperfections in the jelly-roll can have on cell lifetime could encourage the use of X-ray CT in lithium ion cell production.

Acknowledgments

This work was supported by the Engineering and Physical Sciences Research Council [EP/R020973/1, EP/K005030/1, EP/M028100/1]; and the Faraday Institution Degradation, Multiscale Modelling and LiSTAR programmes (FIRG001, FIRG003 and FIRG014 respectively). PRS and JBR acknowledge the support of the Royal Academy of Engineering under CiET1718\59 and ICRF1718\1\34 respectively.

ORCID

Thomas M. M. Heenan https://orcid.org/0000-0001-9912-4772
Dan J. L. Brett https://orcid.org/0000-0002-8545-3126
Paul R. Shearing https://orcid.org/0000-0002-1387-9531
James B. Robinson https://orcid.org/0000-0002-6509-7769

References

1. The Gigafactory Boom: The Demand for Battery Manufacturing in the UK Gifford Stephen (July 2022), Faraday Insights, https://faraday.ac.uk/wp-content/uploads/2022/07/Faraday_Insights_2_update_July_2022_FINAL.pdf.
2. E. Sarasketa-Zabala, F. Aguesse, I. Villarreal, L. M. Rodriguez-Martinez, C. M. López, and P. Kubiak, "Understanding lithium inventory loss and sudden performance fade in cylindrical cells during cycling with deep-discharge steps." *J. Phys. Chem. C*, **119**, 896 (2015).
3. F. Leng, C. M. Tan, and M. Pecht, "Effect of Temperature on the Aging rate of Li Ion Battery Operating above Room Temperature." *Sci. Rep.*, **5**, 12967 (2015).
4. A. Friesen, X. Mönnighoff, M. Börner, J. Haetge, F. M. Schappacher, and M. Winter, "Influence of temperature on the aging behavior of 18650-type lithium ion cells: A comprehensive approach combining electrochemical characterization and post-mortem analysis." *J. Power Sources*, **342**, 88 (2017).
5. G. Ning, B. Haran, and B. N. Popov, "Capacity fade study of lithium-ion batteries cycled at high discharge rates." *J. Power Sources*, **117**, 160 (2003).
6. M. Fleischhammer, T. Waldmann, G. Bisle, B. I. Hogg, and M. Wohlfahrt-Mehrens, "Interaction of cyclic ageing at high-rate and low temperatures and safety in lithium-ion batteries." *J. Power Sources*, **274**, 432 (2015).
7. T. Rauhala, K. Jalkanen, T. Romann, E. Lust, N. Omar, and T. Kallio, "Low-temperature aging mechanisms of commercial graphite/LiFePO4 cells cycled with a simulated electric vehicle load profile—A post-mortem study." *J. Energy Storage.*, **20**, 344 (2018).
8. X. Yang, P. Yang, Z. Zhang, Y. Duan, and J. Hu, "Experimental and numerical study on thermal performance of Li(NixCoyMnz)O2 spiral-wound lithium-ion batteries." *Appl. Therm. Eng.*, **138**, 446 (2018).
9. K. A. Severson et al., "Data-driven prediction of battery cycle life before capacity degradation." *Nat. Energy*, **4**, 383 (2019).
10. Y. Zhang, Q. Tang, Y. Zhang, J. Wang, U. Stimming, and A. A. Lee, "Identifying degradation patterns of lithium ion batteries from impedance spectroscopy using machine learning." *Nat. Commun.*, **11**, 1706 (2020).
11. T. Waldmann, S. Gorse, T. Samtleben, G. Schneider, V. Knoblauch, and M. Wohlfahrt-Mehrens, "A Mechanical Aging Mechanism in Lithium-Ion Batteries." *J. Electrochem. Soc.*, **161**, A1742 (2014).
12. L. K. Willenberg, P. Dechent, G. Fuchs, D. U. Sauer, and E. Figgemeier, "High-precision monitoring of volume change of commercial lithium-ion batteries by using strain gauges." *Sustain.*, **12**, 557 (2020).
13. A. Pfrang, A. Kersys, A. Kriston, D. U. Sauer, C. Rahe, S. Käbitz, and E. Figgemeier, "Geometrical Inhomogeneities as Cause of Mechanical Failure in Commercial 18650 Lithium Ion Cells." *J. Electrochem. Soc.*, **166**, A3745 (2019).
14. A. Pfrang, A. Kersys, A. Kriston, D. U. Sauer, C. Rahe, S. Käbitz, and E. Figgemeier, "Long-term cycling induced jelly roll deformation in commercial 18650 cells." *J. Power Sources*, **392**, 168 (2018).
15. T. C. Bach, S. F. Schuster, E. Fleder, J. Müller, M. J. Brand, H. Lorrmann, A. Jossen, and G. Sextl, "Nonlinear aging of cylindrical lithium-ion cells linked to heterogeneous compression." *J. Energy Storage.*, **5**, 212 (2016).
16. R. Carter, E. J. Klein, R. W. Atkinson, and C. T. Love, "Mechanical collapse as primary degradation mode in mandrel-free 18650 Li-ion cells operated at 0 °C." *J. Power Sources*, **437**, 226820 (2019).
17. R. Carter, B. Huhman, C. T. Love, and I. V. Zenyuk, "X-ray computed tomography comparison of individual and parallel assembled commercial lithium iron phosphate batteries at end of life after high rate cycling." *J. Power Sources*, **381**, 46 (2018).
18. A. S. Mussa, G. Lindbergh, M. Klett, P. Gudmundson, P. Svens, and R. W. Lindström, "Inhomogeneous active layer contact loss in a cycled prismatic lithium-ion cell caused by the jelly-roll curvature." *J. Energy Storage.*, **20**, 213 (2018).
19. J. Cannarella, X. Liu, C. Z. Leng, P. D. Sinko, G. Y. Gor, and C. B. Arnold, "Mechanical Properties of a Battery Separator under Compression and Tension." *J. Electrochem. Soc.*, **161**, F3117 (2014).
20. J. Cannarella and C. B. Arnold, "Ion transport restriction in mechanically strained separator membranes." *J. Power Sources*, **226**, 149 (2013).
21. C. Peabody and C. B. Arnold, "The role of mechanically induced separator creep in lithium-ion battery capacity fade." *J. Power Sources*, **196**, 8147 (2011).
22. J. Cannarella and C. B. Arnold, "The effects of defects on localized plating in lithium-ion batteries." *J. Electrochem. Soc.*, **162**, A1365 (2015).
23. J. Cannarella and C. B. Arnold, "Stress evolution and capacity fade in constrained lithium-ion pouch cells." *J. Power Sources*, **245**, 745 (2014).
24. S. P. V. Nadimpalli, V. A. Sethuraman, D. P. Abraham, A. F. Bower, and P. R. Guduru, "Stress evolution in lithium-ion composite electrodes during electrochemical cycling and resulting internal pressures on the cell casing." *J. Electrochem. Soc.*, **162**, A2656 (2015).
25. J. H. Lee, H. M. Lee, and S. Ahn, "Battery dimensional changes occurring during charge/discharge cycles - Thin rectangular lithium ion and polymer cells." *J. Power Sources*, **119-121**, 833 (2003).
26. X. Wang, Y. Sone, G. Segami, H. Naito, C. Yamada, and K. Kibe, "Understanding volume change in lithium-ion cells during charging and discharging using in situ measurements." *J. Electrochem. Soc.*, **154**, A14 (2006).
27. M. D. R. Kok, J. B. Robinson, J. S. Weaving, A. Jnawali, M. Pham, F. Iacoviello, D. J. L. Brett, and P. R. Shearing, "Virtual unrolling of spirally-wound lithium-ion cells for correlative degradation studies and predictive fault detection, Sustain." *Energy Fuels*, **3**, 2972 (2019).

28. M. Ecker, N. Nieto, S. Käbitz, J. Schmalstieg, H. Blanke, A. Warnecke, and D. U. Sauer, "Calendar and cycle life study of Li(NiMnCo)O2-based 18650 lithium-ion batteries." *J. Power Sources*, **248**, 839 (2014).
29. J. E. Harlow et al., "A wide range of testing results on an excellent lithium-ion cell chemistry to be used as benchmarks for new battery technologies." *J. Electrochem. Soc.*, **166**, A3031 (2019).
30. S. Saxena, C. Le Floch, J. Macdonald, and S. Moura, "Quantifying EV battery end-of-life through analysis of travel needs with vehicle powertrain models." *J. Power Sources*, **282**, 265 (2015).
31. W. Chang, R. Mohr, A. Kim, A. Raj, G. Davies, K. Denner, J. H. Park, and D. Steingart, "Measuring effective stiffness of Li-ion batteries via acoustic signal processing." *J. Mater. Chem. A*, **8**, 16624 (2020).
32. J. B. Robinson, M. Pham, M. D. R. Kok, T. M. M. Heenan, D. J. L. Brett, and P. R. Shearing, "Examining the cycling behaviour of li-ion batteries using ultrasonic time-of-flight measurements." *J. Power Sources*, **444**, 227318 (2019).
33. D. P. Finegan et al., "Spatially resolving lithiation in silicon-graphite composite electrodes via in situ high-energy X-ray diffraction computed tomography." *Nano Lett.*, **19**, 3811 (2019).